IEEE Access
Multidisciplinary | Rapid Review | Open Access Journal

SPECIAL SECTION ON ADVANCED DATA ANALYTICS FOR LARGE-SCALE COMPLEX DATA ENVIRONMENTS

Received October 14, 2017, accepted November 12, 2017, date of publication November 15, 2017,
date of current version February 28, 2018.

Digital Object Identifier 10.1109/ACCESS.2017.2773662

A Sparse Representation Method for *a Priori* Target Signature Optimization in Hyperspectral Target Detection

TING WANG[1], HONGSHENG ZHANG[1,2], (Member, IEEE), HUI LIN[1,2], (Senior Member, IEEE), AND XIUPING JIA[3], (Senior Member, IEEE)

[1]Institute of Space and Earth Information Science, The Chinese University of Hong Kong, Hong Kong
[2]Shenzhen Research Institute, The Chinese University of Hong Kong, Shenzhen 518057, China
[3]School of Electrical Engineering, University College, ADFA, The University of New South Wales, Canberra, ACT 2600, Australia

Corresponding author: Hongsheng Zhang (stevenzhang@cuhk.edu.hk)

This work was supported in part by the National Natural Science Foundation of China under Grant 41401370, in part by the Research Grants Council General Research Fund under Grant CUHK 14601515 and Grant CUHK 14605917, in part by the National Key Basic Research Program of China under Grant 2015CB954103, in part by the Key Laboratory of Spatial Data Mining and Information Sharing of Ministry of Education, Fuzhou University, under Grant 2016LSDMIS02, and in part by the Major Special Project—the China High-Resolution Earth Observation System.

ABSTRACT Many target detectors commonly utilize a single *a priori* target spectral signature as an input. However, the detection results are greatly affected by the quality of the *a priori* target spectral signature because the spectral variability phenomenon is universal and anisotropic in hyperspectral image data. This paper proposes a sparse representation-based method to generate an optimized target spectrum from limited target training samples, which is able to alleviate the impact of spectral variability on hyperspectral target detection. When lacking comprehensive knowledge about the target object of interest, an optimized representative target spectrum should be expected to be reconstructed by the hyperspectral data themselves in a sparse representation manner following the characteristics of the data structure and then be generated by a set of selected candidate pixels that contain the target signal with a varying status. With the optimized *a priori* target signature, the experimental results of the detection of different characteristics of objects with three different types of hyperspectral images confirm the effectiveness, robustness, and generality performance of the proposed method.

INDEX TERMS Target detection, spectral variability, sparse representation.

I. INTRODUCTION

The spectral features in hyperspectral imagery (HSI) contain a significant structure that, if fully exploited, could enable more efficient data acquisition and improved data analysis [1]. The band design differs from multispectral sensors — not only in the way it continuously covers wider wavelength ranges but also the diagnostic spectral curves it provides by corresponding to each type of material. The spectral imaging modality of HSI that contains environmental and geographical information can be adaptively utilized to extract varied types of information that can be only obtained by special design in multispectral sensors [2].

Exploiting HSI has been declared to be extremely challenging due to the particularly complicated remote sensing environment [3]. One of the most widespread perceived challenges on an image scene is that even so-called pure pixels that are supposed to be composed of a single material would have reflectance spectra that lie in a nonlinear space or is manifold due to variations in illumination, view angle, material heterogeneity, scattering from the local scene geometry, and the presence of moisture [4], [5]. In actual hyperspectral imaging scenes, pure pixels are impossible to actually observe due to the material mixtures within a pixel and scattering from adjacent areas due to its method of collecting energetic signal. This problem causes barriers to execution of many hyperspectral image processing tasks [6] and is especially severe for a target detection task that distinguishes few target pixels from the overwhelming number of background pixels [7].

Generally speaking, most state-of-the-art target detectors rely on the quality of the a priori information about the targets, but obtaining such information is difficult due to the noise

signal [8], [9], the spectral variation, and the sub-pixel target phenomenon [10]. Noise removal had been widely studied and is not the main issue in this paper. Sub-pixel targets arise from the fact that the ground sampling distance is usually larger than the size of the targets of interest due to the limitations of the spatial resolution of the hyperspectral imaging sensors [11], [12]. The spectral variation phenomenon refers to the reflectance spectrum of a certain desired material; although this spectrum is supposed to be unique, multiple factors can introduce spectral variability to a particular material [13]. Some references had also reported that sub-pixel targets can be considered another form of spectral variability [14]. Focusing on the spectral variation phenomenon including the contribution piece of the sub-pixel caused, the ideal circumstance is that detectors are successfully applied to HSI target detection tasks based on the premise that the target endmember can be accurately estimated and unmixed [15]. This means that a unique representative point in the high-dimensional data space should be selected to account for the pure signature of an interested target object. The actual situations, however, that are most representative of an a priori target spectrum can scarcely be found. Many factors may be responsible for the variability of obtained target spectra: un-compensated sensor errors, un-calibrated atmospheric deviation, environmental effects, surface containment, and adjacency effects, in which reflections from nearby objects in the scene will deteriorate the uniqueness of the target signature [16]–[18].

For most traditional detection tasks, a spectrum of interested target objects from an existing target spectral library is an expedient choice. However, the gap between the spectrum of a target in spectral library and one on the real scene prevents the wide use of the spectral library [19]. When lacking a usable spectral signature for a specific material, direct selection from the hyperspectral image is the sole, albeit inferior, choice to obtain the a priori target signature. The advantage of image endmembers is that they can be collected at the same scale as the image and are easier to associate with image features [20]. However, this requires a very strict and robust selection procedure to obtain relatively high-quality information about the a priori information of targets. All these discussed factors will greatly restrict the quality of an a priori target signature that can be obtained, consequently limiting the performance of target detectors.

To address the spectral variability problem, several successful detectors had been developed by expanding the dimensionality of the a priori target signature. Orthogonal subspace projection (OSP) separates a space composed of desired spectral signals from the undesired spectra [21]. Matched subspace detectors (MSD) provided invariant approaches for signal detection using hypothesis tests based on linear subspace mixture models [22]. An invariant material identification method based on the maximum likelihood estimation had also been developed to address the spectral variability through the use of a comprehensive physical model to capture the dependence of the reflected sunlight, the reflected skylight, and path-radiance terms on the scene geometry and on the distribution of atmospheric gases and aerosols over a wide range of conditions [10]. A nonlinear support vector data description (SVDD) method can characterize the target class's spectral variation from a single pure target training sample with the Markov model [23]. These methods have been verified to effectively address the spectral variability problem to some degree, but their performances will still be affected by the quality and quantity of the available set of training target pixels, which is rare and precious in practical cases. Moreover, these methods were obviously not appropriate for detectors that rely on a single target spectrum, such as the Adaptive Coherence Estimator (ACE) [24], Matched Filter (MF), Constrained Energy Minimization (CEM) [21] and Adaptive Matched Filter (AMF). For one of the most commonly used detectors, ACE, using a single target spectrum or an average of the candidate target spectra from the image was routine. Due to the effect of the spectral variability, a highly qualified single a priori target spectrum is badly needed in practical cases for these detectors. To summarize, the current methods of acquiring the a priori target spectrum are not sufficient to obtain the optimum detection results. There is a clear need for research on how to use available data and minimum prior knowledge to optimize the crucial target signature from limited or even a single target training sample to address the spectral variation mentioned above and reduce the detection error probability to the best possible outcome.

The spectrum optimization method had been rarely discussed in previous research because most studies have focused on the design of detectors. It should be clearly noted that if the provided training sample for target detectors is inaccurate, the estimation bias of a given detector is unavoidable. Some researchers had already noticed this bottleneck for HSI target detection and made some attempts toward obtaining higher quality a priori target information. An automatic, robust, iteratively reweighted spectrum generation method for an unstructured detector had been proposed to produce satisfactory detection performance from a random chosen a priori target spectrum [25]. The method used all available spectra regarding possible target candidates to adaptively converge to an optimized a priori target signature. The computational costs and convergence issues cannot be omitted as it is an iterative algorithm and followed a common approach to determine whether the material present in a given pixel is spectral un-mixing. The vectors forming a convex hull with the involved HSI data are called endmembers, which presents unique spectral signatures of the various material components in the scene. In the data processing society, a number of methods had been proposed for determining endmembers, including algorithms that selected endmembers from the data based on a measure of pixel purity [26] or the quality of the resulting convex cone [27], tools that assisted in the manual selection of endmembers from the data [28], algorithms that optimized endmembers for linear filtering [29], methods based on finding convex cones using

principal component analysis (PCA) decompositions [30], iterative statistical methods that optimized the resulting convex cone [31], and iterative measures to select optimal endmember sets from larger potential sets [32]. However, these algorithms basically assumed the existence of pure pixels in the scene and consequently attempt to encompass the data within a cone rather than directly represent the data variations. For the unusual event of a target detection task, in which a scarce training sample could be obtained to describe the statistical and distributional features of this certain class, none of these methods attempt to directly exploit a good representation of the low-dimensional, non-linear spectral variations inherent in the HSI data [1].

The signal processing community had recently employed signal models based on the notion of sparsity to characterize high-order statistical dependencies in data, which is accurately suitable for HSI representation [33]. The sparsity-based HSI representation models can be depicted as a pixel vector expressed by a linear combination of just a few elements from a given set of vector dictionaries, where the coefficients are calculated to have as few non-zero elements as possible. This can be considered as a way to search for the intrinsic dimensionality of HSI as another version of a common approach PCA (Principal Component Analysis). Contradictorily, PCA assumes the Gaussianity of the data, which means its incapability in capturing high-order and non-Gaussian statistics is present in the HSI data [34]. Sparse coding models can express a point in a high dimensional dataset with the lower dimensional space of active coefficients. As the PCA calculates only a few principal components and uses essentially all of them to represent each pixel, sparse coding models typically employ a much larger dictionary but use unfixed elements to represent each pixel. When considering in terms of a probabilistic model, the sparsity constraint corresponds to a non-Gaussian prior that enables the model to be more flexible to capture higher order statistics in the data.

With the gradual high spatial resolution of HSI sensors, the sparsity model had been reported to be especially relevant for describing the structure of the data as the amount of dominant materials being small in a vector, which coincides with the case of high spatial resolution hyperspectral data. Initial research using sparsity models for spectral un-mixing has shown promising results, as stated in [35]. These sparse representation-based methods leverage the specific high-order statistics of the example dataset to find the underlying low-dimensional structure that is most efficient at representing the data [36], [37]. To effectively and generally search for the most representative spectral feature of under-detected materials from unknown data — because intrinsic endmembers may be sparsely represented — when the a priori target signature is uncertain, part of the data points with the higher likelihood of target candidates are expected to probe and analyze following a sparse representation manner for addressing the bottleneck of the HSI target detection.

The remainder of the manuscript is organized as follows. Section II analyses the spectral variability phenomenon, and the proposed sparse representation-based a priori target signature optimization algorithm is detailed. The experimental design that considers performance improvement, practicability, robustness and generality about the proposed algorithm in three real hyperspectral datasets is presented in Section IV. Finally, conclusions are drawn in Section V.

II. METHOD

A. SPECTRAL VARIABILITY

As discussed in the introduction, target detection algorithms are usually applied in a single radiometrically corrected hyperspectral image. Therefore, the spectral variability caused by the sensor, atmosphere, and seasonal changes are not considered in this manuscript. To summarize: the main contribution to the spectral variability phenomenon in target detection tasks lies in two facets: interior factors and exterior factors.

Exterior factors incorporate all spectral changes created by the surrounding materials and observation deviations caused by topographical and surface roughness during the sensor imaging process. It is easy to understand that different man-made objects may have different degrees of surface roughness, which will directly affect the reflectance intensity of the electromagnetic waves. For hyperspectral images with either high or low spatial resolution, spectral mixing is universal. In low spatial resolution images, disparate materials jointly occupy a single pixel such that the pixel is composed of several individual spectra [38]. In this circumstance, when the spectrum of the pixel is selected as the target signature, it cannot accurately represent the characteristics of the target material. The spectral variability caused by spectral mixing is commonly resolved using a spectral un-mixing procedure. Spectral mixing is inevitable, not only for low spatial resolution images, but even for high spatial resolution images because mixed pixels can result when distinct materials are combined together into an intimate mixture in the same area. Furthermore, when multiple bounces are caused by the intimate components or a rough surface, the spectral variability ultimately presents a nonlinear characteristic [39]. As the mixing process can sometimes be quite complicated, many algorithms have been developed to un-mix the hyperspectral data with different mixing assumptions, including geometrical, statistical, and sparse regression based approaches [40], [41]. As the target pixels are very rare in the image, the endmembers extracted from the image may not include the desired target, and, if included, the spectrum may not satisfy the accuracy required for target detection [42].

Interior factors, also called intrinsic factors, are engendered by the target materials themselves. The size of particles, the texture of composites, and variation in the material such as age-induced colour fading and uneven material components will all lead to various spectral characteristics of one single object. For example, it is common that materials are composites, especially for artificial objects, where the uneven proportions of different ingredients cause spectral variability.

The difference caused by the aging of materials can also be a problem, which leads to material deteriorating and colour fading. Finally, the surface may be contaminated by an unknown pollutant, such as paints in different colours or unexpected animals, etc. Because these factors are hard to predict and estimate in a model, few studies have addressed this problem and offered efficient solutions.

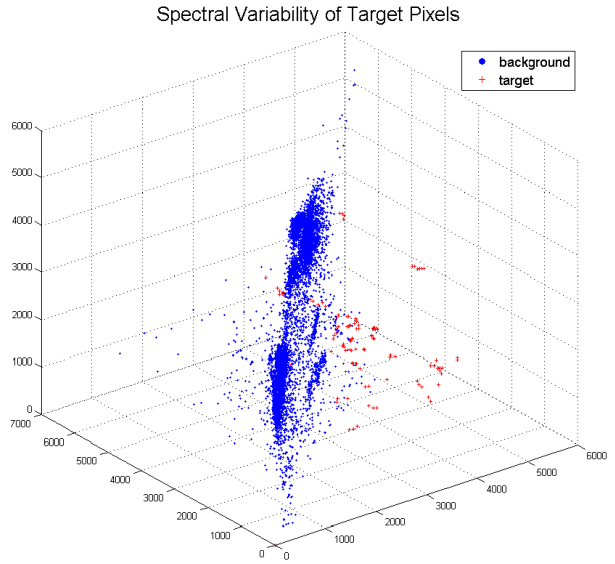

FIGURE 1. Distribution of the spectral characteristics of target candidates.

A visual map is utilized to describe how serious the spectral variability will impede the successful detection of the candidate target pixels in a real hyperspectral image scene. A total of 116 pixels of the target are selected from a hyperspectral image cube, which will be introduced in the experiment section. The digital number of values of three individual bands of all the background pixels and the target pixels, which are shown in blue filled dots and red cross marks, respectively, are shown in Figure 1. The diagram reflects the distribution features of the spectral characteristics of the pixels in the hyperspectral image scene, which, in most detectors, will be treated as the only input feature. Due to the spectral variability phenomenon, the scattered target pixels display a distribution status of being non-identical and non-Gaussian.

The most representative point needs to be selected from these red cross points to be treated as an a priori target signature for detectors. Obviously, the distribution of target candidates illustrates the difficulty in searching for a qualified candidate when there is a lack of previous knowledge. Furthermore, a simple demonstration of the bias of detection performance caused by the a priori target spectrum is then shown in Figure 2.

Four candidates that could be treated as the a priori target spectrum are carefully selected from the image, which come from different sections of the target objects in different illumination conditions. Figure 2 is a schematic plot of how and how seriously a randomly selected a priori target signature can impact the final detection performance by a certain detector, ACE. It can be easily seen that the four detection maps have obvious biases in the tendency to present higher detection scores for the pixels that are in a more similar condition or are much closer to the pre-selected a priori target spectrum. This is especially dangerous when a hasty decision has to be made when lacking prior knowledge of the target of interests, as is the case in the last blue frame with the target signature selected from location (89,11), which is even seemingly a wise choice from the main body of the target object. What this spectral variability problem has shown here is the fact that detection performance is commonly not expected to correspondingly reflect the desired similarities between the target objects and a chosen representative target spectrum in the scene.

B. THE SPARSITY-BASED A PRIORI TARGET SPECTRUM OPTIMIZATION METHOD

Considering the complicated contributing factors of spectral variability in target detection, it is not impossible to present categorized solutions that are specialized for many reasons. Methods of adequately exploiting the intrinsic connections of the data point themselves and adaptively adjusting the bias of a random input of the target signature remains a significant challenge for the target detection task. This would not be practical in actual cases as spectral variation reasons should be analysed accurately in advance. In this paper, an algorithm is designed to optimize the a priori target signature from a spectral variability-suffered spectrum to consequently obtain satisfactory and stable detection performance from different target signatures with glaring discrepancies. Because the detection results are seriously susceptible to the a priori target signature, a practical, stable and general algorithm should be proposed that fully considers the characteristics of the hyperspectral data structure.

The basic assumption is that the various forms of target candidates have already existed in different statuses on the image scene, which is always true. Our work is to find the different statuses of the targets and use them to optimize a more representative a priori target signature. Each pixel of the hyperspectral image is composed of only several types of endmembers, and the sparsity model has been reported to be especially relevant for describing the structure of the data because the number of dominant materials is small in a vector. This advantage could be leveraged when using the sparse representation model to describe a given vector. All the other descriptive vectors should wholly or partly cover some extent of the status of the given vector. These vectors are all related in a sparse space, where an elaborate combination of the vectors is expected to better cover all the possible status of the target object of interest. The spectral variability problem should be alleviated, and better target detection performance should be obtained.

Figure 3 depicts the whole workflow of the proposed sparsity-based target spectra optimization method. From the original HSI data and some specific targets of interest, such

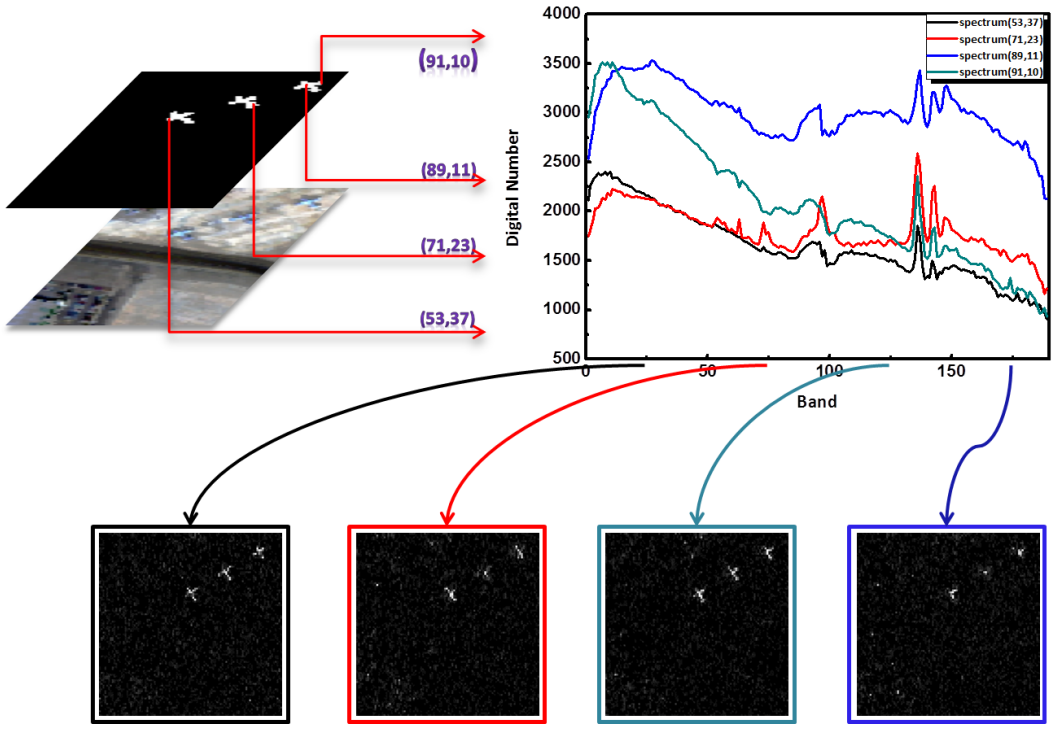

FIGURE 2. Bias of detection performance from different targets a priori.

as the airplane located on the upper right corner, a random input of the target spectrum as a priori information is selected for an initial detection. The intensity map shows the possibilities that each pixel may contain the signal of an interested target. There are a certain number of pixels that have greater possibilities than the others according to the random input of the target spectrum, which is circled in black. These candidate pixels are selected for construction of an overcomplete dictionary whose atoms are descriptive vectors that wholly or partly cover the different status of the given target signature. This dictionary is expected to sparsely represent each potential target pixel vector. Fewer high score pixels are then marked out, and for each of them, a coefficient vector can be derived with the mentioned fixed sparse code dictionary. The coefficient vectors are sparse vectors with a few nonzeros and mostly zeros. The location of those that correspond to the contributed pixels in the given target spectrum on the scene and their emergence frequencies reflect their weights. After the solutions of all the coefficient vectors are presented, a vote procedure is adopted to determine the frequency of the existence of these potential target pixels. Eventually, pixels with top frequencies are chosen to re-construct the refined a priori target spectrum, and the final detection result is then given.

1) HYPERSPECTRAL TARGET DETECTOR

ACE is a benchmark detector that has been proved to be effective with a single target spectrum [42]. Because there is no single best detector [44], ACE is taken as an example of the matched filter type detectors. Differing from the structured background model based detectors, the unstructured background models do not need explicit a priori information about the background, which makes the spectral variability problem simplified here, only focusing on the target spectral optimization. For a given hyperspectral pixel vector, when the additive noise is included in the background matrix B, the competing hypotheses between the target and non-target pixel are:

$$\begin{aligned} H_0&: \boldsymbol{x} = \boldsymbol{b}, \quad \boldsymbol{b} \sim N(0, \Gamma) \text{ Target absent} \\ H_1&: \boldsymbol{x} = \boldsymbol{S\alpha}_t + \boldsymbol{b}, \quad \text{Target present} \end{aligned} \tag{1}$$

where the S matrices are the target signatures and α_t is the corresponding abundance contained in the target pixels. If there is no target abundance in the pixel, it can be described with b, which is modelled by a multivariate normal distribution with a zero mean and covariance matrix Γ.

With the implication of the generalized likelihood ratio approach, Kelly obtained the famous detector, known as Kelly's GLRT [24]:

$$D_{KGLRT}(\boldsymbol{x}) = \frac{\boldsymbol{x}^T \tilde{\boldsymbol{\Gamma}}^{-1} \boldsymbol{S} \cdot \left(\boldsymbol{S}^T \tilde{\boldsymbol{\Gamma}}^{-1} \boldsymbol{S}\right)^{-1} \cdot \boldsymbol{S}^T \tilde{\boldsymbol{\Gamma}}^{-1} \boldsymbol{x}}{N + \boldsymbol{x}^T \tilde{\boldsymbol{\Gamma}}^{-1} \boldsymbol{x}} \tag{2}$$

where $\tilde{\Gamma}$ represents the estimation of the covariance matrix from the data and N is the number of the total pixels in the image. If the value of pixel x is beyond a given threshold η, it is assigned to the target class. However, in the hypotheses

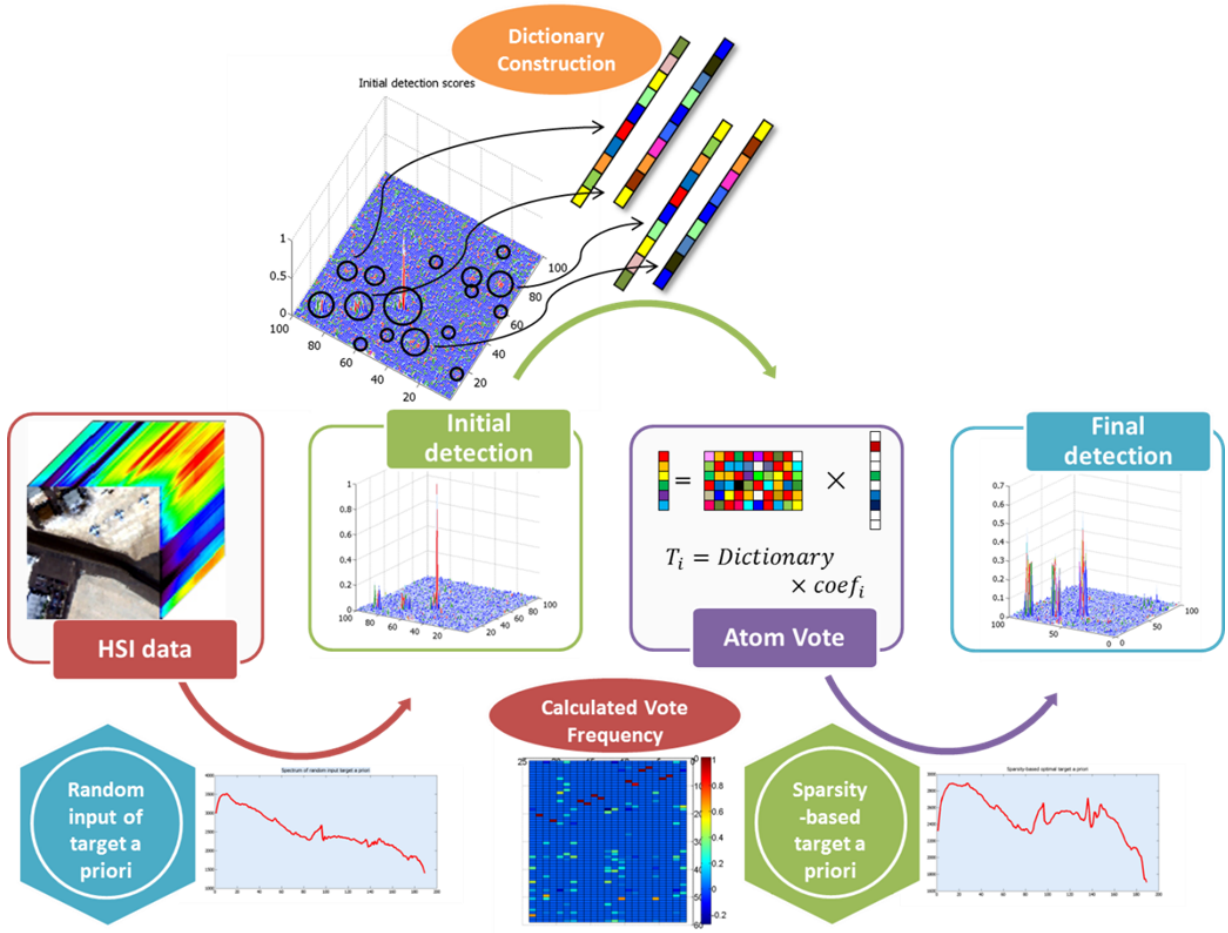

FIGURE 3. Flowchart of the sparsity-based target spectra generation method.

above, the covariance matrix of the background is the same under the H_0 and H_1 hypotheses, which is not accurate in most cases [22]. In other words, to be more accurate, the background statistic of a pixel with or without the target signal should be different. Thus, the background has the same covariance structure but different variance, and this variance is directly related to the fill factor of the target, i.e., the percentage of the pixel area occupied by the target object. Therefore, the competing hypotheses are more appropriately written as

$$\begin{aligned} H_0 &: \boldsymbol{x} = \boldsymbol{b}, \quad \text{Target absent} \\ H_1 &: \boldsymbol{x} = \boldsymbol{S\alpha}_t + \sigma\boldsymbol{b}, \quad \text{Target present} \end{aligned} \tag{3}$$

where $x \sim N(0, \Gamma)$ under H_0 and $x \sim N(S\alpha, \sigma^2\Gamma)$ under H_1. The different variance is related to the percentage of target pixels in the image, considering the effect of the target in proportion to the alteration of the covariance matrix of the background, which is the impact of the parameter σ. Kraut [45] developed the ACE detector. Here, the matrix S contains the available a priori variability information about the target, and $\tilde{\boldsymbol{\Gamma}}$ represents the estimated covariance matrix from the data, which is usually calculated from the whole image:

$$D_{ACE}(\boldsymbol{x}) = \frac{\boldsymbol{x}^T\tilde{\boldsymbol{\Gamma}}^{-1}\boldsymbol{S}\cdot\left(\boldsymbol{S}^T\tilde{\boldsymbol{\Gamma}}^{-1}\boldsymbol{S}\right)^{-1}\cdot\boldsymbol{S}^T\tilde{\boldsymbol{\Gamma}}^{-1}\boldsymbol{x}}{\boldsymbol{x}^T\tilde{\boldsymbol{\Gamma}}^{-1}\boldsymbol{x}}. \tag{4}$$

The ACE detector is taken as an exemplar algorithm to validate the effectiveness of the optimization method. The generality in the experiment section validating the ACE detector in the workflow could be replaced by other benchmark detectors because only detection scores from the detector is crucial for the following steps.

2) SPARSE REPRESENTATION

The randomly chosen target signature s should then be sparsely represented by pixels with high detection scores, which will wholly or partly cover some extent of the status of the given signature. In fact, the ideal a priori target signature must lie in high dimensional space that is spanned by all other statuses of the potential target pixels. The structure of the mentioned spanned space is totally unknown due to the discussed complicated factors, such as the imaging scene and the attributes of the desired targets. Therefore, the space could either be linearly or nonlinearly described, while the

sparse representation shows good performance for the data description when they are in an unknown manifold.

The substantial correlation among hyperspectral bands and pixels determine the sparse characteristics of hyperspectral data. This coincides with the sparsity-based techniques, which have been proposed for many hyperspectral processing fields such as classification, un-mixing, facial recognition, dimensionality reduction and target detection [46]–[50]. Studies in [51] for the first time explores both the statistics and sparsity features to propose an integrated hybrid hypothesis based sub-pixel detector, which proves more effective than state-of-the-art sparsity detection methods. Given a pixel $\boldsymbol{s} \in \mathbb{R}^N$ and a predefined fixed dictionary $\{\boldsymbol{\phi}_k\}$ with $\boldsymbol{\phi}_k \in \mathbb{R}^N$ for $k \in [1, \ldots, M]$, the goal of sparse coding is to find a set of coefficients that represents each of the potential target candidates using as few non-zero elements as possible. More specifically, each previously chosen target pixel $\boldsymbol{s}$can be modelled to be situated in a dictionary that is made of the union of all the potential candidate pixels:

$$\boldsymbol{s} = \boldsymbol{\Phi\alpha} \tag{5}$$

where Φ can be spanned by M pixels existing in the image that contains a target signal with a different degree and status and whose rows are the measurement vectors. For $D_{ACE}(x_i) > T_b$, x_i is recorded as one of the M pixels. M should be determined by a detection score threshold, which is noted as T_b. $\alpha = \{\alpha_1, \alpha_2, \ldots, \alpha_M\}$ is the corresponding coefficient of the M pixels involved, also known as the sparse vector. From a mathematical point of view, the goal is to minimize an objective function that combines data fidelity and a sparsity-inducing penalty. A common choice is to use a regularized least-squares objective function, such as

$$J_\gamma\left(x, \{\boldsymbol{\alpha}_k\}, \{\boldsymbol{\phi}_k\}\right) = \left\| \boldsymbol{s} - \sum_{k=1}^{M} \boldsymbol{\phi}_k \boldsymbol{\alpha}_k \right\|_2^2 + \gamma \sum_{k=1}^{M} |\boldsymbol{\alpha}_k| . \tag{6}$$

With a mean-squared error as the data fidelity term, the l^1 norm (i.e., the sum of the coefficient magnitudes) as the sparsity inducing penalty, and with γ as a scalar parameter switching off between these two terms [52]. This optimization is convex in the coefficients when the dictionary is fixed, meaning that solving the simplified l^0 optimization problem stated in Equation (7) is:

$$\hat{\boldsymbol{\alpha}} = argmin \|\boldsymbol{\Phi\alpha} - \boldsymbol{s}\|_2 , \quad s.t. \ \|\boldsymbol{\alpha}\|_0 \le \delta_0 \tag{7}$$

where $\|\cdot\|_0$ denotes the l_0 norm, which is defined as the number of nonzero entries in the vector, also known as the sparsity level of the vector. δ_0 is a given upper bound on the sparsity level. A classic way to obtain a sparse representation is through a greedy algorithm, the most famous of which is an orthogonal matching pursuit (OMP) [53]. It has been proven by [54] and [55] that under certain conditions, the OMP can find the sparsest representation of the signal.

Followed by the sparse representation statement, to identify the ideal signal α, we need to determine which column of Φ participates in the measurement vector s. The idea is to pick columns in a greedy fashion. In each iteration, OMP chooses the column of Φ that is most strongly correlated with the remaining part of s. The OMP subtracts its contribution to s and iterates in the residual. One hopes that after p iterations, the algorithm will have identified the correct set of columns.

The inputs of algorithm OMP include 1) an N × M measurement matrix Φ (the dictionary constructed by T_b); 2) an N–dimensional data vector s; and 3) the sparsity level q of the ideal signal. The expected output of the OMP includes 1) an estimate $\hat{\alpha}$ in $\mathbb{R}^d$ for the ideal signal (the location of the contributed atoms); 2) a set Λ_m containing q elements from $\{1, \ldots, d\}$; 3) an N–dimensional approximation $\hat{s}_p$ of the data s; and 4) an N–dimensional residual $r_p = s - \hat{s}_p$.

The procedure is described as follows.

1) Initialize the residual $\boldsymbol{r}_0 = \boldsymbol{s}$, the index set $\Lambda_0 = \Phi$, and the iteration counter $t = 1$.
2) Find the index λ_t that solves the easy optimization problem
$$\lambda_t = \text{argmax}_{j=1,\ldots,d} \left| \langle \boldsymbol{r}_{t-1}, \boldsymbol{\varphi}_j \rangle \right| \tag{8}$$
If the maximum occurs for multiple indices, break the tie deterministically.
3) Augment the index set and the matrix of chosen atoms:
$$\begin{aligned} \Lambda_t &= \Lambda_{t-1} \bigcup \{\lambda_t\} \\ \boldsymbol{\Phi}_t &= \left[\boldsymbol{\Phi}_{t-1} \boldsymbol{\varphi}_{\lambda_t}\right] \end{aligned} \tag{9}$$
We use the convention that $\boldsymbol{\Phi}_0$ is an empty matrix.
4) Solve a least squares problem to obtain a new signal estimate:
$$\boldsymbol{\alpha}_t = \text{argmin}_x \|\boldsymbol{s} - \boldsymbol{\Phi}_t \boldsymbol{\alpha}\|_2 \tag{10}$$
5) Calculate the new approximation of the data and the new residual:
$$\begin{aligned} \hat{\boldsymbol{s}}_t &= \boldsymbol{\Phi}_t \boldsymbol{\alpha}_t \\ \boldsymbol{r}_t &= \boldsymbol{s} - \hat{\boldsymbol{s}}_t \end{aligned} \tag{11}$$
6) Increment t and return to Equation (8) if $t < p$.
7) The estimate $\hat{\boldsymbol{\alpha}}$ for the ideal signal has nonzero indices in the components listed in Λ_q. The value of the estimate $\hat{\boldsymbol{\alpha}}$ in component λ_j equals the jth component of $\boldsymbol{\alpha}_t$.

Steps 4, 5, and 7 have been written to emphasize the conceptual structure of the algorithm so that they can be implemented more efficiently. It is important to recognize that the residual $\boldsymbol{r}_t$ is always orthogonal to the columns of $\boldsymbol{\Phi}_t$. Provided that the residual $\boldsymbol{r}_{t-1}$ is nonzero, the algorithm selects a new atom at iteration t, and the matrix $\boldsymbol{\Phi}_t$ has a full column rank. In this case, solution $\boldsymbol{\alpha}_t$ to the least squares problem is Step 4 is unique.

3) OPTIMIZATION OF THE A PRIORI TARGET SIGNATURE

Threshold T_b is used to select enough candidate target pixels $\Phi = \{\phi_1, \phi_2, \ldots \phi_M\}$ to construct a sparse dictionary that covers the possible status of different forms of target pixels.

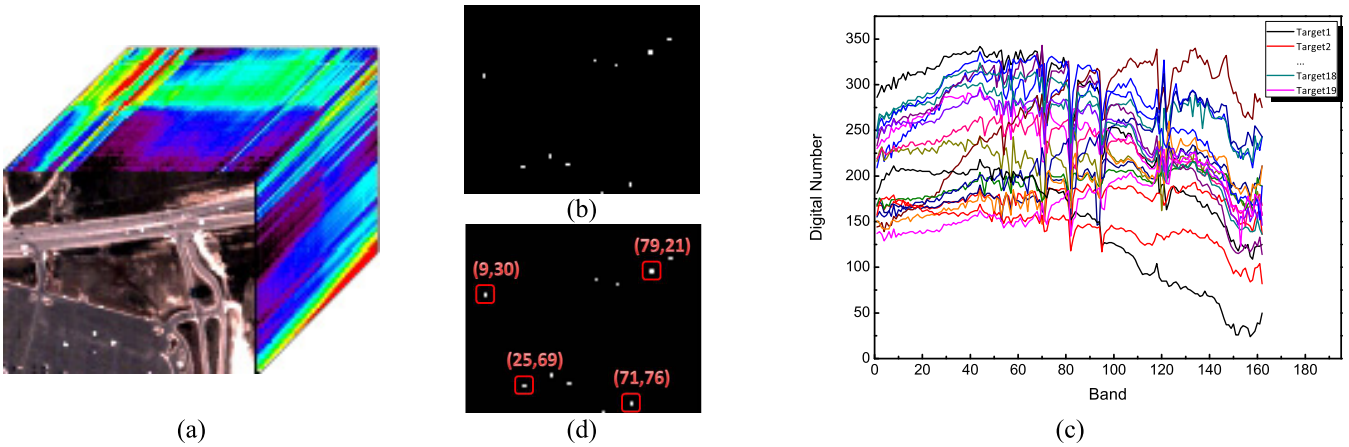

FIGURE 4. The HYDICE dataset: (a) hyperspectral cube; (b) true location of the targets; (c) spectral curves of the different target pixels; and (d) selected random chosen target a priori.

Another set of pixels that are much more likely to contain the target signal is then determined by a larger threshold T_a. For $D_{ACE}(x_i) > T_a$, each pixel closely approximates to the initial a priori target spectrum. The set can be described as candidate pixels set $\Omega = \{\omega_1, \omega_2, \ldots, \omega_N\}$ to optimize the target signature, which can be spanned by N pixels. The initial pixel is excluded as the weight should be 1. Each pixel in Ω can then be sparsely represented by the calculated dictionary Φ.

$$\hat{\boldsymbol{\alpha}} = argmin \|\boldsymbol{\Phi\alpha} - \boldsymbol{s}\|_2, \quad s.t. \ \|\boldsymbol{\alpha}\|_0 \leq \delta_0. \tag{12}$$

The sparse vector β_k of N pixel in Ω accurately embodies the contribution of each vector in Φ to the given target spectrum. The locations of nonzero elements in the sparse vector β_k are crucial to optimize the a priori target signature. A vote procedure is introduced here to decide the weight of each atom in the dictionary, indicated as the frequency that ϕ_k occurs in sparsely representing ω_k, where the frequencies are recorded as ε_k of each ω_k. The weighted average of their original spectral vector in Φ is then computed by

$$\boldsymbol{s}_{\text{final}} = \sum_{k=1}^{N} \boldsymbol{\omega}_k \varepsilon_k / \sum \varepsilon_k. \tag{13}$$

With this optimized target spectrum $\boldsymbol{s}_{final}$, the final detection result with a detector will be given.

III. EXPERIMENT ANALYSIS

The spectral variability phenomenon is universal to all remote imaging sensors in all types of scenes; therefore this proposed target spectra optimization method is significant and practical once it is proven to be efficient and robust. Three HSI datasets from different sensors and imaging environments had been used to validate the proposed sparsity-based optimized target a priori generation method. Four aspects were expected and passed through the whole experimental design: 1) the promotion of the detection performance of a particular type of material; 2) the robustness of the optimizing process from a random input a priori target spectrum; 3) sensitivity analysis about the relevant parameter and discussion about practicability; and 4) the generality and adaptability of the proposed algorithm to various types of sensors, scenes, and detectors.

A. HYPERSPECTRAL DATASETS

The three datasets came from different hyperspectral sensors, including AVIRIS (Airborne Visible/Infrared Imaging Spectrometer), HYDICE (Hyperspectral Digital Imagery Collection Experiment), and the Nuance Hyperspectral Imaging System. The HYDICE image dataset covering an urban area and the main materials were roads, public squares, vegetation, and bare soil, as shown in Figure 4. The HYDICE imaging sensor generated 210 bands covering the whole spectral range of 400–2500 nm, but only 162 spectral bands were used after discarding the water absorption and low-SNR bands. The spatial resolution was 4 m and the vehicles were selected as the targets to detect. The difficulties in this detection task lay in the fact that most of the under-detected pixels were sub-pixel targets due to the spatial resolution and target size (the target is about the same size as the pixel). Nineteen pixels were chosen as the references for the target locations according to their similarities to the spectrum of the vehicle targets [56], as shown in Figure 4(b). Figure 4(c) showed all the curves of the 19 pixels that contained the target signal. They presented quite different statuses due to the spectral variability phenomenon, as mentioned before. We chose four of them, which were randomly located at (9,30), (25,69), (71,76) and (79,21) on the image for the a priori target input.

The San Diego image was collected by AVIRIS, an airborne sensor covering a naval air station in San Diego, California. The colour image is shown in Figure 5 (a). A total of 189 bands remained after removing the water absorption bands and low-SNR bands, covering a wavelength range of 0.4–1.8 . The spatial resolution was 3.5 m and the image was mainly composed of buildings with manmade impervious infrastructure, such as different types of buildings, parking aprons of different materials, an airport runway, and a small quantity of vegetation. We chose the airplanes as the

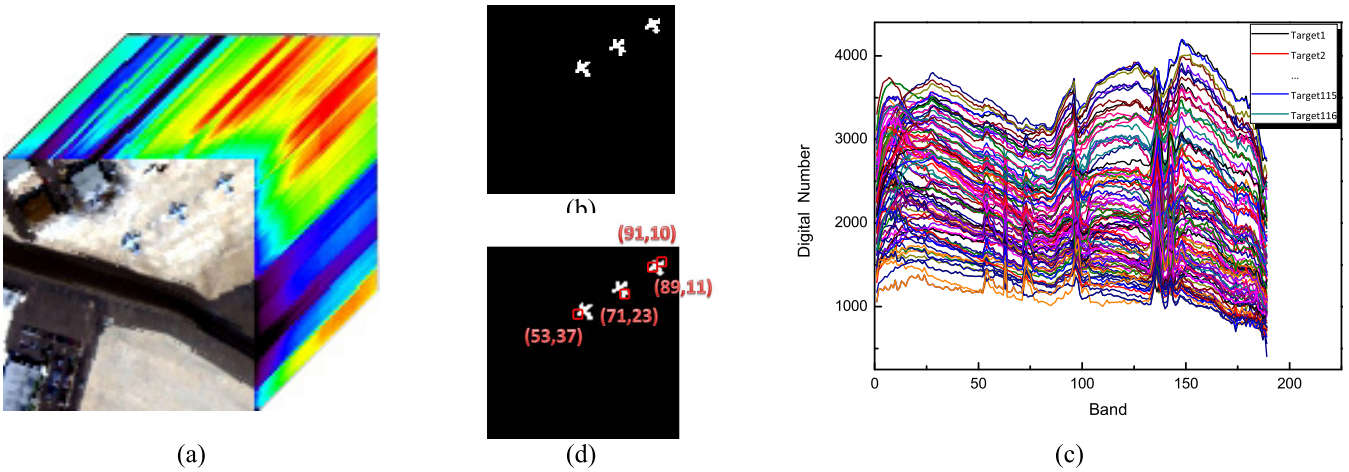

FIGURE 5. AVIRIS dataset: (a) hyperspectral cube; (b) true location of the targets; (c) spectral curves of the different target pixels; and (d) selected random chosen target a priori.

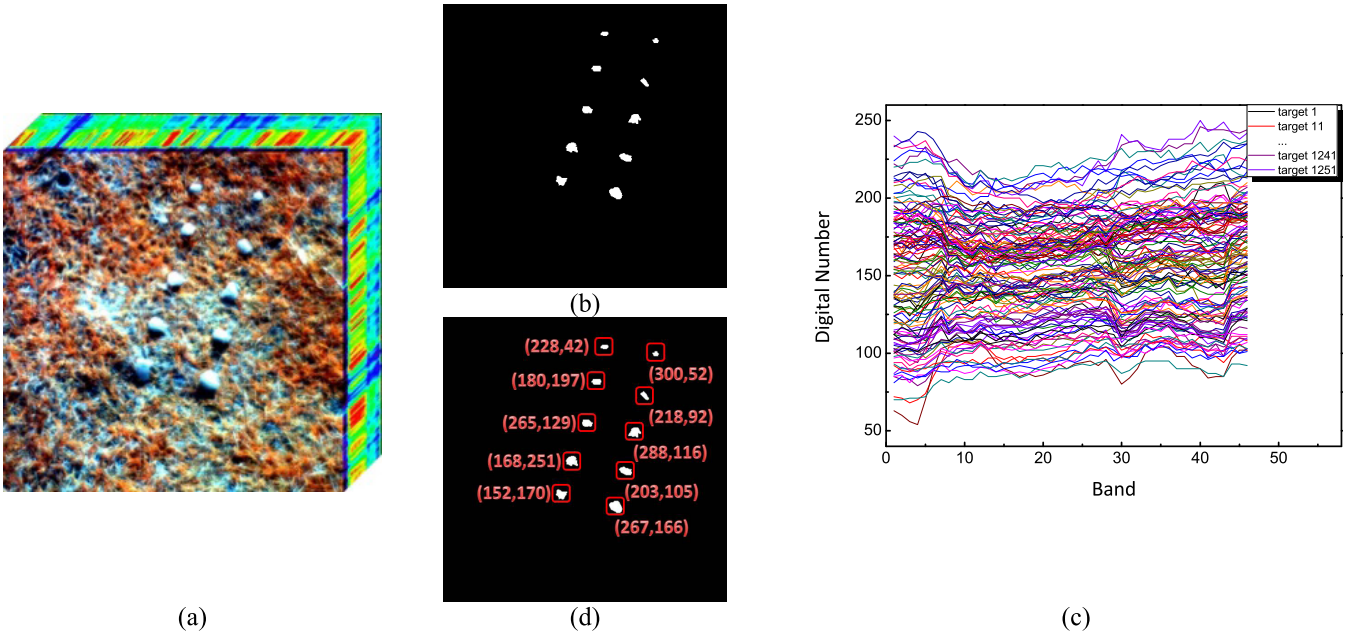

FIGURE 6. Nuance dataset: (a) hyperspectral cube; (b) true location of the targets; (c) spectral curves of the different target pixels; and (d) selected random chosen target a priori.

targets for detection. The location of the targets is shown in Figure 5 (b). In total, 116 pixels were selected as targets, which were composed of full-pixel targets in the main body of the airplanes and sub-pixel targets on the edges of the airplanes. The difficulties in this detection task lay in that full-pixel and sub-pixel targets simultaneously existed in the scene. The sub-pixel targets on the edge of the airplane body were affected either by being spectrally mixed with the reflection of the parking aprons or the multi-scattering phenomenon between the airplane body and surroundings. As shown in Figure 5 (c), the spectra of the 116 pixels greatly differ from each other, even for the full-pixel targets in the centre of the three airplanes. Therefore, there was a deliberate choice of 4 random inputs of the target a priori covering the main body (89,11), right wing (91,10), left wing (53,37) and tail of the airplane (71,23), respectively, as shown in Figure 5 (d).

The third real hyperspectral dataset was acquired by the Nuance Hyperspectral Imaging System. This sensor can acquire imagery with a spectral resolution of less than 10 nm, and the spectral imaging range covers 650 to 1100 nm. Because it is a hand-held device, the imaging scope is quite narrow, and the spatial resolution is approximately 0.01 m, considering the current focal length. As a result, we used a small-scale scene with comparatively smaller targets deployed in the scene. In detail, ten stones of varying sizes were located in the grass scene to simulate the circumstances of full-pixel targets, and the false colour image is shown in Figure 6 (a). The difficulties in this detection task lay in the fact that although all the candidates in this scene

TABLE 1. AUC values of different parameter combinations in AVIRIS dataset.

T_a \ T_b	0.01	0.02	0.03	0.04	0.05	0.06	0.07	0.08	0.09	0.1
0.02	0.7317									
0.03	0.7886	0.8498								
0.04	0.8261	0.8750	0.9096							
0.05	0.8398	0.8849	0.9207	0.9544						
0.06	0.8461	0.8948	0.9260	0.9581	0.9588					
0.07	0.8632	0.9064	0.9303	0.9592	0.9608	0.9599				
0.08	0.8697	0.9148	0.9326	0.9605	0.9604	0.9600	0.9626			
0.09	0.8694	0.9095	0.9306	0.9591	0.9620	0.9568	0.9618	0.9725		
0.1	0.8597	0.9000	0.9210	0.9582	0.9587	0.9543	0.9601	0.9726	0.9712	
0.11	0.8632	0.8997	0.9147	0.9612	0.9556	0.9523	0.9577	0.9725	0.9713	0.9683
0.12	0.8649	0.9013	0.9072	0.9581	0.9540	0.9506	0.9565	0.9731	0.9715	0.9679
0.13	0.8524	0.8760	0.9111	0.9558	0.9531	0.9564	0.9575	0.9706	0.9664	0.9637
0.14	0.8312	0.8628	0.9021	0.9481	0.9402	0.9450	0.9436	0.9664	0.9645	0.9632
0.15	0.8316	0.8841	0.8984	0.9464	0.9328	0.9383	0.9414	0.9685	0.9618	0.9628
0.16	0.8316	0.8841	0.8984	0.9464	0.9328	0.9383	0.9414	0.9685	0.9618	0.9628
0.17	0.8316	0.8841	0.8984	0.9464	0.9328	0.9383	0.9414	0.9685	0.9618	0.9628
0.18	0.8519	0.8316	0.8902	0.9468	0.9383	0.9496	0.9540	0.9668	0.9610	0.9609
0.19	0.8519	0.9002	0.8902	0.9468	0.9383	0.9496	0.9540	0.9668	0.9610	0.9609
0.2	0.8366	0.8710	0.8846	0.9352	0.9397	0.9296	0.9400	0.9494	0.9610	0.9529

were full-pixel targets, the spectral variability phenomenon was exhibited in different ways, including complicated illuminations caused by directions to the light, bumpy surface of the most ordinary stones, as well as the imaging quality of the sensor with no radiometric calibration. The spectral variability of all 1254 target pixels was even more serious. As a display of more than 1200 spectra is difficult to interpret, the spectra of the 254 target candidate pixels were downsized to a scale of 126 spectra in every 10 pixels, as shown in Figure 6 (c). Ten typical random selected targets a priori were labelled and shown in Figure 6 (d).

B. EXPERIMENT PARAMETER SETTINGS

There are two parameters in the workflow. Corresponding to T_b, B is the number of pixels that compose the dictionary, and corresponding to T_a, A is the number of pixels that is selected for the statistics to generate the new target signature. For the AVIRIS dataset, we had adopted an exhaustive method to test all the combinations of these two parameters within a certain range.

As the candidate pixels were selected from the dictionary pixels, the value of parameter A should be set as larger than that of B. After obtaining all the detection results from the given parameters, the ROC (Receiver Operating Characteristic) curves can be drawn according to the actual distribution of the targets. Because there were too many curves that were difficult to visually interpret, the AUC (Area Under Curve) values were calculated by an integration method. Table 1 shows the detailed AUC values under different detection circumstances with a varied combination of these two parameters. The AUC value table shows good detection performance gain in general, while the peak of the AUC value appears at the combination of 0.08 and 0.12. These AUC statistics given by exhaustion method of different parameter combination is only designed to convince the audience that the results are not sensitive to the choice of these parameters, and the performance could be maintain at a relatively high level when dedicated choosing progress of parameters is missing.

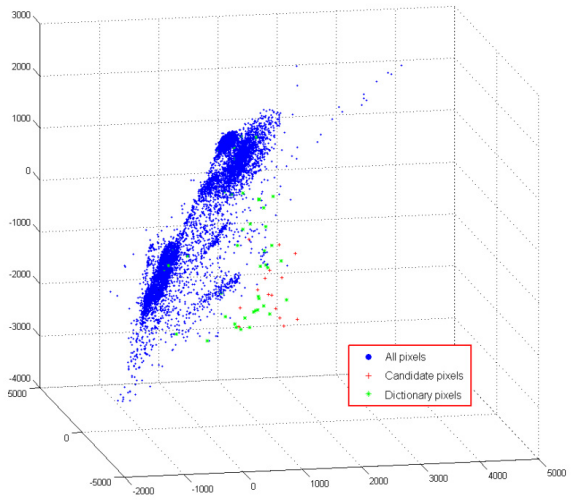

FIGURE 7. Locations of the selected candidate and dictionary pixels in the original data space.

Take the detection scenario of $T_a = 0.12$, $T_b = 0.08$ as an example, where the details about the relative experiments are displayed. According to these particular parameters, the number of candidate pixels is 20 and the number of dictionary pixels is 79. From Figure 7, the locations of the selected candidate and dictionary pixels out of all the pixels were

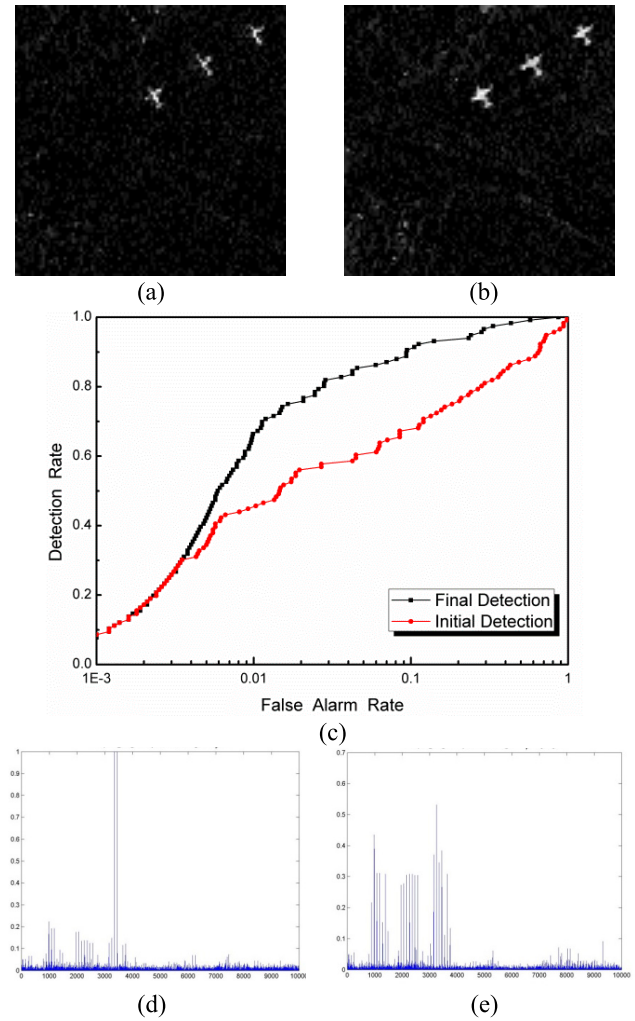

FIGURE 8. Detection performance improvement before and after the algorithm. (a) Initial detection. (b) Final detection. (c) ROC curves. (d) Initial detection scores. (e) Final detection scores

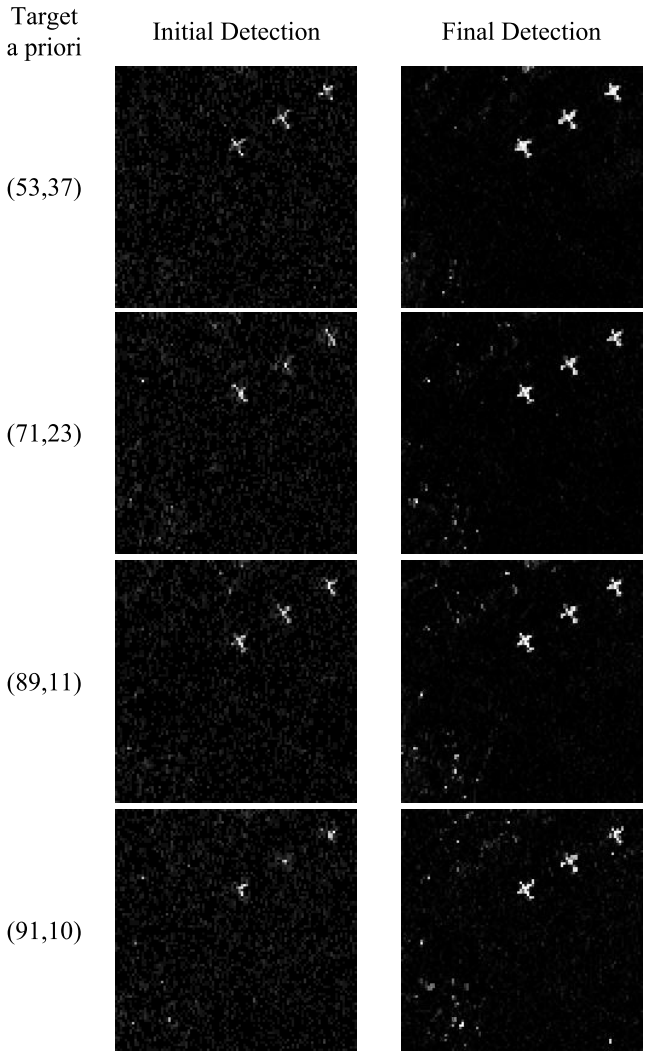

FIGURE 9. Robustness test of randomly chosen targets a priori in the AVIRIS image.

displayed in original data space for a directly perceived purpose. The points with green asterisks were the pixels that are related to the initial target a priori, which also composed the dictionary to sparsely represent the initial spectral signature, while the red cross marks were the pixels that will be voted for significance and are consequently utilized to optimize the optimal target a priori.

The parameter setting for dictionary pixels and candidate pixels substantially reflect the pixels that are going to be used in the optimization process. Either too few or too many pixels is not appropriate for dictionary construction because too few pixels will be inadequate to cover all the statuses of the target signal, while too many pixels will have repeated statuses, consequently impacting the frequency calculated in the generation of the final a priori target signature. A wise decision here is to use a parameter that can select a dictionary pixel set with number that is no larger than the real target pixels and a parameter that determines a candidate pixel set of an even smaller size, e.g., one or two dozen.

With these candidate pixels, the optimal spectrum target a priori can be generated. The comparison between the initial and final detection performance was illustrated in Figure 8. For a better visual effect, the detection performances in Figure 8 (a) and (b) were enhanced in a square root manner by ENVI software. The corresponding detection scores were displayed in Figure 8 (d) and (e), which clearly illustrated the improvement of the detection. The generated target a priori has a comprehensive consideration of all the target pixels in different conditions and therefore yields a more balanced detection score of all the pixels of the aircraft body. The ROC curves in Figure 8 (c) also reflected the generated target signature's superiority to the original one because the final detection curve occupies the upper location entirely.

C. ROBUSTNESS ANALYSIS

Another significant issue of this proposed algorithm is the robustness, i.e., whether a relatively stable detection outcome can be derived from a series of random inputs of targets

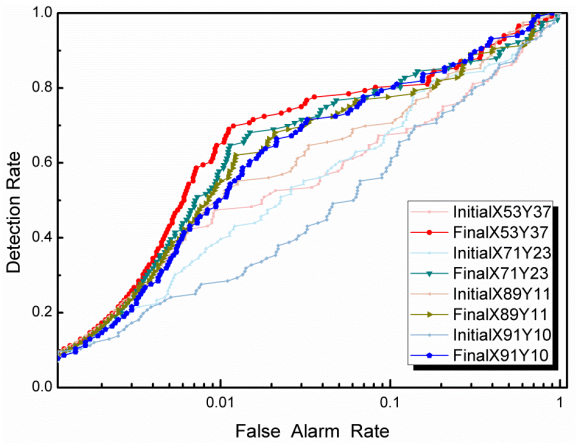

FIGURE 10. ROC curves of the detection performance improvement from randomly chosen targets a priori in the AVIRIS image.

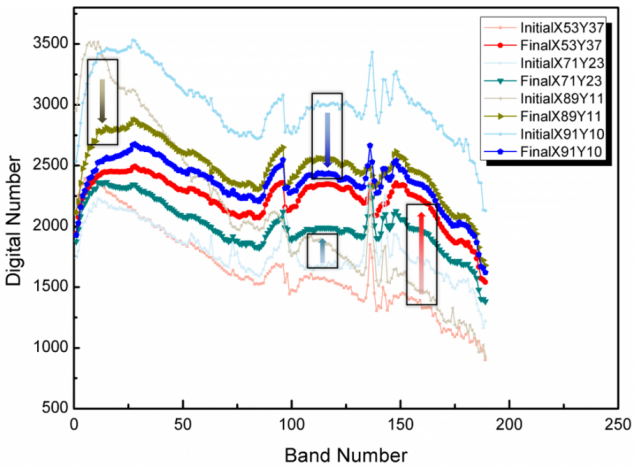

FIGURE 11. Spectra curves of the target a priori before and after the algorithm.

a priori. As has been stated in Section 3.1, four distinguished locations of the image target a priori were selected to validate the robustness of the proposed target spectrum generation method. The four image spectra came from different parts of the planes, which greatly varied from each other and would generate partial detection results if they were directly placed into the detector, as shown in Figure 9. After using the same parameter setting as in the previous section, the proposed algorithm is capable of alleviating these random selected deviations as in cases (53, 37), (71, 23), and (89, 11). Even for the badly chosen target a priori (91, 10), the initial detection result showed its strong incapability, while the generated target spectrum could amend the consequences caused by the bad choice.

ROC curves had been drawn in four pairs, corresponding to the initial and final detection performance of each circumstance of the four inputs. The lighter curves in the colour scheme were the detection performance by the initial target spectra, while the darker curves corresponded to the detection results after improving the target signature. It can obviously be seen that the performances all substantially improved.

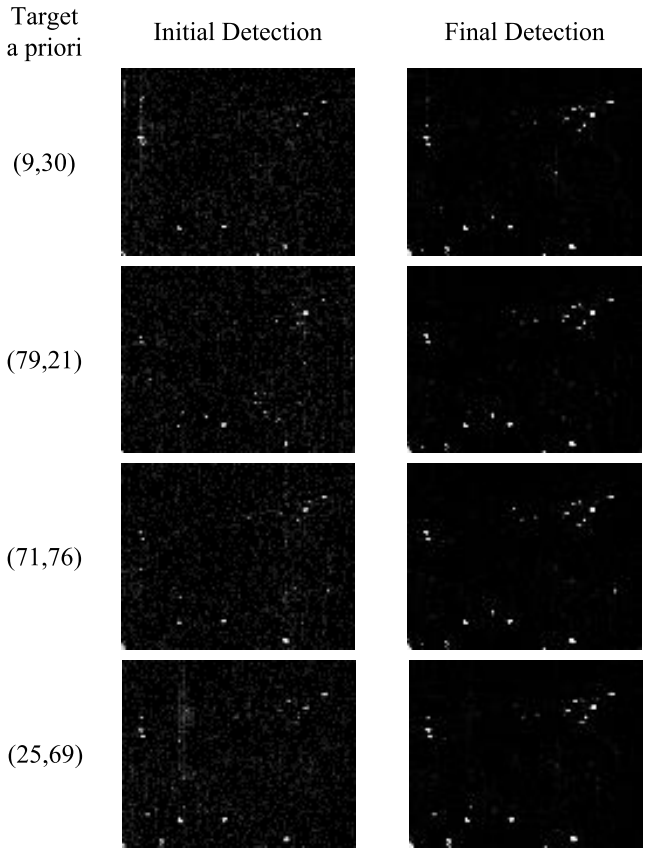

FIGURE 12. Robustness test of randomly selected target a priori in the HYDICE image.

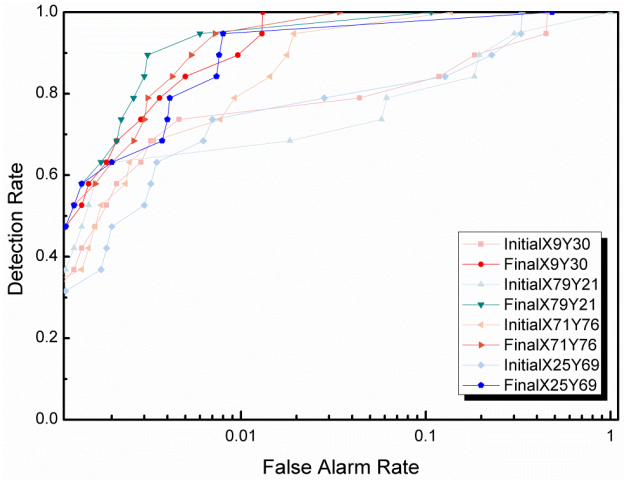

FIGURE 13. ROC curves of the detection performance improvement in HYDICE image.

Regardless of the initial quality of the target a priori, relatively good ones targets such as (89,11) and (53,37), or even an unsound one such as (91,10) — which is on the wing edge of the airplane, where the spectrum can easily being mixed with other materials — the enhancements are remarkable. This experiment had validated the practicability of the proposed algorithm when the choice of the image target signature is inexperienced and arbitrary, which is common

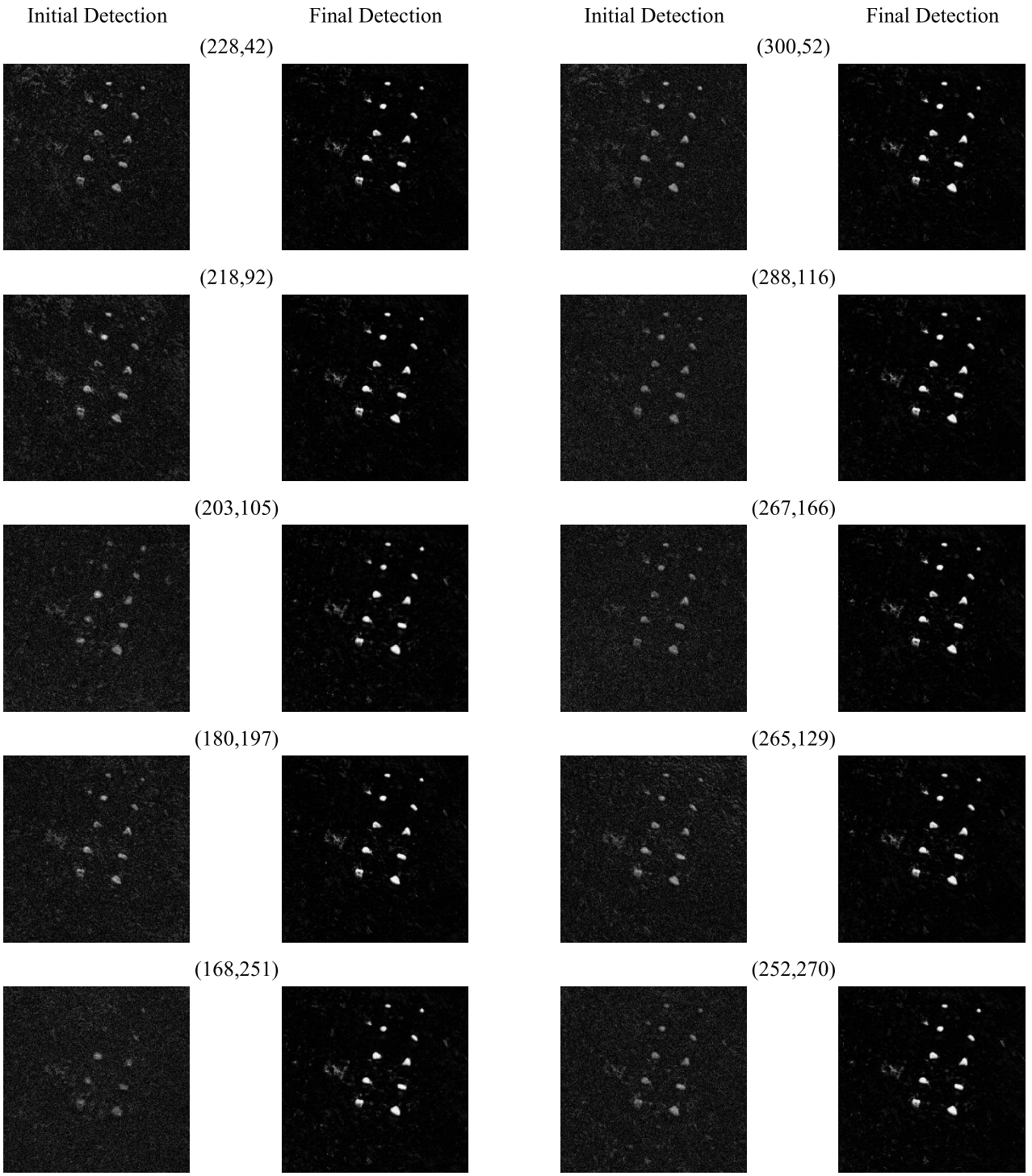

FIGURE 14. Robustness test of randomly selected targets a priori in the Nuance image.

when there is a lack of comprehensive expertise regarding the task.

To further reveal the mechanism of the proposed method, the generated spectra from these four initial targets a priori were recorded and drawn in Figure 11. For a clear presentation, the initial spectra were marked with a series of tint colours, while the final spectra were marked in dark paired colour. Four arrows were labelled to vividly describe the change of the target signature. The general features of the spectra had been well maintained, such as the peaks and troughs; some were amended to some extent, while small fluctuations and anomalies had been moved to make the target feature smoother. Broadly speaking, the four generated spectra from the random input reached a similar outcome from an optimal target a priori.

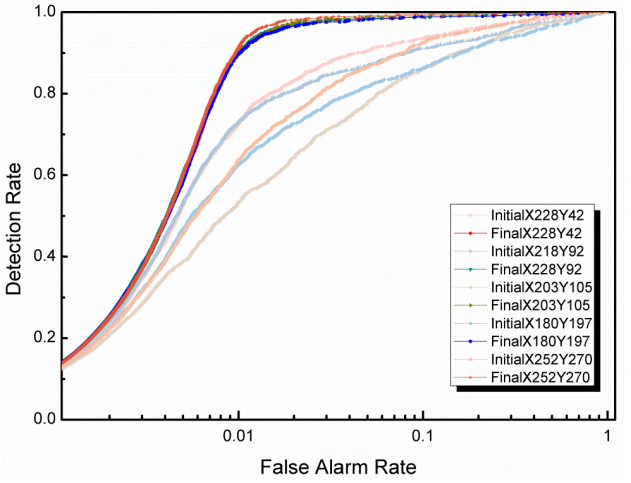

FIGURE 15. ROC curves of the detection performance improvement in the Nuance image.

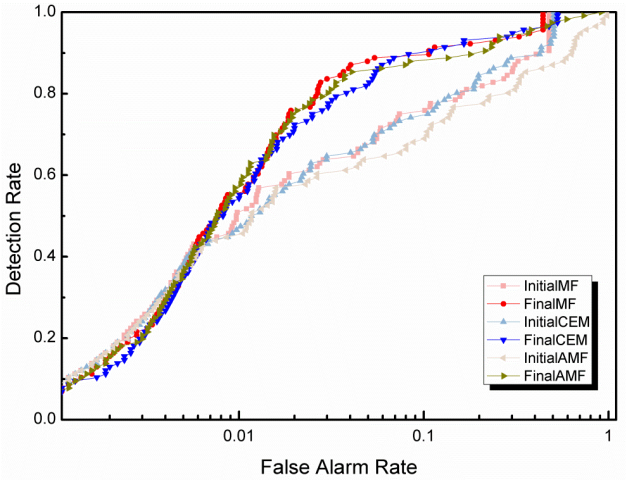

FIGURE 17. ROC curves of the detection performance improvement using several benchmark detectors.

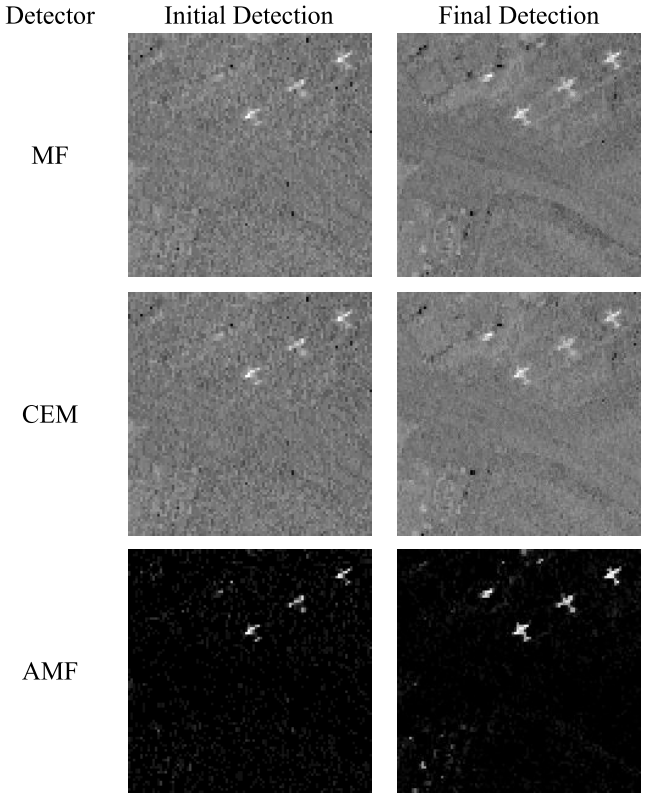

FIGURE 16. Tests on different detectors with sparse representation-based target a priori optimized method.

D. DETECTION PERFORMANCE OF GENERALITY

Since the effectiveness and robustness of the proposed algorithm have been validated, its generality in other hyperspectral datasets should also be tested. The HYDICE and Nuance datasets mentioned in Section 3.1 were utilized to further confirm the algorithm with other sensors and imaging environments. Because the spectral variability phenomenon is universal and anisotropic, for the airborne and handheld sensors, the phenomenon is still important but in different ways. Taking the intrinsic data characteristics into consideration, the proposed algorithm should have a satisfactory performance of generality when utilizing other dataset and circumstances.

Figure 12 showed the initial and final detection results obtained by the original target a priori and optimized target a priori, respectively. The parameters for T_a and T_b were set as 0.1 and 0.06 following the principle of controlling the size of the dictionary set and candidate set. Because the targets under detection were vehicles on this image, the target spectra varied from the colour of the cars, the material quality of the cars, the subpixel proportion of car body in the pixels and the mixed spectra due to different objects on which the cars are located. The noise signals were strong in the initial detection because knowledge about the vehicle targets was rare, while the optimized target signature gave stable detection results regardless of the data that had been initially placed in the detector.

ROC curves further certified their growth in detection performance. Most targets can be recognized within a 1% false alarm rate.

The Nuance dataset had been acquired in a handheld manner, which experienced a relative straightforward imaging path. However, the variability caused by the sensors and image background still seriously impacted the detection of the stone. Ten pixels of the image spectrum had been selected from the body of the stone, respectively, to be treated as inputs of the ACE detector.

The parameters for T_a and T_b were set as 0.2 and 0.1 following the same principle. As shown in Figure 14, the column of initial detection exhibited a pattern in which the initial signal of the target a priori input was not strong enough to represent all the target pixels in the image. The optimized target signature, however, made the target distinctly separate from the background. Five out of the ten pairs of ROC curves had been drawn to quantitatively reflect the enhancement of

the detection performance, where the curves in light colours corresponded to the original performance and their counterparts in dark colours were the results after optimization.

E. ALGORITHM PORTABILITY

The proposed method for the optimized target a priori generation is further expected to have stable portability when adopted in other hyperspectral target detectors. Some benchmark detectors had been therefore listed in Figure 16, and their detection performances with and without the sparse representation-based optimized targets a priori were also displayed. The benchmark detectors include the most frequently used MF, CEM and AMF.

Visual interpretation had proved that the capability and feasibility of the proposed algorithm was not limited to the ACE detector. The contribution of this optimization method does not solely embody improvement of certain detector designs but also a class of detectors.

This is especially significant to conclude its practicability in other application scenes. The sparse characteristic has generally existed in hyperspectral data, which results in an innovative use of this representation in an ideal way to optimize the substantial form of the target a priori. With these higher quality target signatures, the ROC curves were obtained, which were marked in darker colours in Figure 17, which had surpassed the ones in lighter colours obtained from the original target a priori. The improvements were obvious and no extra knowledge was required, making this algorithm very practical.

IV. CONCLUSIONS

The quality of the a priori target signature is the bottleneck of target detection tasks from hyperspectral imagery. If the provided training sample for target detectors is inaccurate, the estimation bias of a given detector is unavoidable, regardless of how advanced the detectors are being designed. The proposed sparse representation-based a priori target signature optimization method can quickly and effectively generate a relatively high-quality spectrum as an input for a series of detectors. The experimental results for three real hyperspectral datasets with varied sensors and scenes have validated its capability of enhancing the detection performance, as well as giving robust results when placed into different a priori target signatures. However, it works under the assumption that the interested target exists in the scene thereby the initial choose will be somewhat related to the true spectra of the target. For future studies, the proposed algorithm can be further generalized and test to other detectors as it purifies the target priori before designing any detectors. Exploiting the sparse characteristics of hyperspectral data and intrinsic feature of the target spectra could alleviate the uncertainties caused by target spectral variability, consequently overcoming the mentioned bottleneck. If the parameters could be adaptively calculated instead of a referential value, with no additional data needed, it will make the algorithm more practical and promising in widespread application.

REFERENCES

[1] A. S. Charles, B. A. Olshausen, and C. J. Rozell, "Learning sparse codes for hyperspectral imagery," *IEEE J. Sel. Topics Signal Process.*, vol. 5, no. 5, pp. 963–978, Sep. 2011.
[2] D. Manolakis, D. Marden, and G. A. Shaw, "Hyperspectral image processing for automatic target detection applications," *Lincoln Lab. J.*, vol. 14, no. 1, pp. 79–116, 2003.
[3] F. D. van der Meer and S. M. de Jong, Eds., *Imaging Spectrometry: Basic Principles and Prospective Applications*. Springer, 2011.
[4] C. M. Bachmann, T. L. Ainsworth, and R. A. Fusina, "Exploiting manifold geometry in hyperspectral imagery," *IEEE Trans. Geosci. Remote Sens.*, vol. 43, no. 3, pp. 441–454, Mar. 2005.
[5] J. P. Kerekes and J. R. Schott, "Hyperspectral imaging systems," in *Hyperspectral Data Exploitation: Theory and Applications*. Hoboken, NJ, USA: Wiley, 2007, pp. 19–45.
[6] J. Li *et al.*, "Multiple feature learning for hyperspectral image classification," *IEEE Trans. Geosci. Remote Sens.*, vol. 53, no. 3, pp. 1592–1606, Mar. 2015.
[7] S. Matteoli, M. Diani, and J. Theiler, "An overview of background modeling for detection of targets and anomalies in hyperspectral remotely sensed imagery," *IEEE J. Sel. Topics Appl. Earth Observ. Remote Sens.*, vol. 7, no. 6, pp. 2317–2336, Jun. 2014.
[8] N. Acito, M. Diani, and G. Corsini, "Signal-dependent noise modeling and model parameter estimation in hyperspectral images," *IEEE Trans. Geosci. Remote Sens.*, vol. 49, no. 8, pp. 2957–2971, Aug. 2011.
[9] B. Du and L. Zhang, "A discriminative metric learning based anomaly detection method," *IEEE Trans. Geosci. Remote Sens.*, vol. 52, no. 11, pp. 6844–6857, Nov. 2014.
[10] Q. Du and C.-I. Chang, "A signal-decomposed and interference-annihilated approach to hyperspectral target detection," *IEEE Trans. Geosci. Remote Sens.*, vol. 42, no. 4, pp. 892–906, Apr. 2004.
[11] G. Healey and D. Slater, "Models and methods for automated material identification in hyperspectral imagery acquired under unknown illumination and atmospheric conditions," *IEEE Trans. Geosci. Remote Sens.*, vol. 37, no. 6, pp. 2706–2717, Nov. 1999.
[12] B. Du and L. Zhang, "Random-selection-based anomaly detector for hyperspectral imagery," *IEEE Trans. Geosci. Remote Sens.*, vol. 49, no. 5, pp. 1578–1589, May 2011.
[13] J. Zhang, B. Rivard, A. Sánchez-Azofeifa, and K. Castro-Esau, "Intra- and inter-class spectral variability of tropical tree species at La Selva, Costa Rica: Implications for species identification using HYDICE imagery," *Remote Sens. Environ.*, vol. 105, no. 2, pp. 129–141, 2006.
[14] G. A. Shaw and H.-H. K. Burke, "Spectral imaging for remote sensing," *Lincoln Lab. J.*, vol. 14, no. 1, pp. 3–28, 2003.
[15] A. Zare and K. Ho, "Endmember variability in hyperspectral analysis: Addressing spectral variability during spectral unmixing," *IEEE Signal Process. Mag.*, vol. 31, no. 1, pp. 95–104, Jan. 2014.
[16] B. Demir, F. Bovolo, and L. Bruzzone, "Detection of land-cover transitions in multitemporal remote sensing images with active-learning-based compound classification," *IEEE Trans. Geosci. Remote Sens.*, vol. 50, no. 5, pp. 1930–1941, May 2012.
[17] M. Herold, D. A. Roberts, M. E. Gardner, and P. E. Dennison, "Spectrometry for urban area remote sensing—Development and analysis of a spectral library from 350 to 2400 nm," *Remote Sens. Environ.*, vol. 91, nos. 3–4, pp. 304–319, 2004.
[18] J.-P. Combe *et al.*, "Analysis of OMEGA/Mars express data hyperspectral data using a multiple-endmember linear spectral unmixing model (MELSUM): Methodology and first results," *Planetary Space Sci.*, vol. 56, no. 7, pp. 951–975, 2008.
[19] F. van der Meer, "The effectiveness of spectral similarity measures for the analysis of hyperspectral imagery," *Int. J. Appl. Earth Observat. Geoinf.*, vol. 8, no. 1, pp. 3–17, 2006.
[20] T. Rashed, J. R. Weeks, D. Roberts, J. Rogan, and R. Powell, "Measuring the physical composition of urban morphology using multiple endmember spectral mixture models," *Photogramm. Eng. Remote Sens.*, vol. 69, pp. 1011–1020, Sep. 2003.
[21] J. C. Harsanyi and C.-I. Chang, "Hyperspectral image classification and dimensionality reduction: An orthogonal subspace projection approach," *IEEE Trans. Geosci. Remote Sens.*, vol. 32, no. 4, pp. 779–785, Jul. 1994.
[22] L. L. Scharf and B. Friedlander, "Matched subspace detectors," *IEEE Trans. Signal Process.*, vol. 42, no. 8, pp. 2146–2157, Aug. 1994.
[23] W. Sakla, A. Chan, J. Ji, and A. Sakla, "An SVDD-based algorithm for target detection in hyperspectral imagery," *IEEE Geosci. Remote Sens. Lett.*, vol. 8, no. 2, pp. 384–388, Mar. 2011.

[24] E. J. Kelly, "An adaptive detection algorithm," *IEEE Trans. Aerosp. Electron. Syst.*, vol. AES-22, no. 2, pp. 115–127, Mar. 1986.
[25] T. Wang, B. Du, and L. Zhang, "An automatic robust iteratively reweighted unstructured detector for hyperspectral imagery," *IEEE J. Sel. Topics Appl. Earth Observ. Remote Sens.*, vol. 7, no. 6, pp. 2367–2382, Jun. 2014.
[26] A. Plaza, P. Martinez, R. Perez, and J. Plaza, "Spatial/spectral endmember extraction by multidimensional morphological operations," *IEEE Trans. Geosci. Remote Sens.*, vol. 40, no. 9, pp. 2025–2041, Sep. 2002.
[27] M. E. Winter, "N-FINDR: An algorithm for fast autonomous spectral end-member determination in hyperspectral data," *Proc. SPIE*, vol. 3753, pp. 266–275, Oct. 1999. [Online]. Available: https://www.spiedigitallibrary.org/conference-proceedings-of-spie/3753/1/N-FINDR–an-algorithm-for-fast-autonomous-spectral-end/10.1117/12.366289.full
[28] A. Bateson and B. Curtiss, "A method for manual endmember selection and spectral unmixing," *Remote Sens. Environ.*, vol. 55, no. 3, pp. 229–243, 1996.
[29] J. H. Bowles, P. J. Palmadesso, J. A. Antoniades, M. M. Baumback, and L. J. Rickard, "Use of filter vectors in hyperspectral data analysis," *Proc. SPIE*, vol. 2553, pp. 148–157, Sep. 1995. [Online]. Available: https://www.spiedigitallibrary.org/conference-proceedings-of-spie/2553/1/Use-of-filter-vectors-in-hyperspectral-data-analysis/10.1117/12.221352.full
[30] A. Ifarraguerri and C. I. Chang, "Multispectral and hyperspectral image analysis with convex cones," *IEEE Trans. Geosci. Remote Sens.*, vol. 37, no. 2, pp. 756–770, Mar. 1999.
[31] M. Berman, H. Kiiveri, R. Lagerstrom, A. Ernst, R. Dunne, and J. F. Huntington, "ICE: A statistical approach to identifying endmembers in hyperspectral images," *IEEE Trans. Geosci. Remote Sens.*, vol. 42, no. 10, pp. 2085–2095, Oct. 2004.
[32] D. M. Rogge, B. Rivard, J. Zhang, and J. Feng, "Iterative spectral unmixing for optimizing per-pixel endmember sets," *IEEE Trans. Geosci. Remote Sens.*, vol. 44, no. 12, pp. 3725–3736, Dec. 2006.
[33] M. Elad, M. A. T. Figueiredo, and Y. Ma, "On the role of sparse and redundant representations in image processing," *Proc. IEEE*, vol. 98, no. 6, pp. 972–982, Jun. 2010.
[34] X. Jia and J. A. Richards, "Segmented principal components transformation for efficient hyperspectral remote-sensing image display and classification," *IEEE Trans. Geosci. Remote Sens.*, vol. 37, no. 1, pp. 538–542, Jan. 1999.
[35] M.-D. Iordache, J. Bioucas-Dias, and A. Plaza, "Sparse unmixing of hyperspectral data," *IEEE Trans. Geosci. Remote Sens.*, vol. 49, no. 6, pp. 2014–2039, Jun. 2011.
[36] B. Du, M. Zhang, L. Zhang, R. Hu, and D. Tao, "PLTD: Patch-based low-rank tensor decomposition for hyperspectral images," *IEEE Trans. Multimedia*, vol. 19, no. 1, pp. 67–79, Jan. 2017.
[37] L. Zhang, L. Zhang, D. Tao, X. Huang, and B. Du, "Compression of hyperspectral remote sensing images by tensor approach," *Neurocomputing*, vol. 147, pp. 358–363, Jan. 2015.
[38] N. Keshava and J. F. Mustard, "Spectral unmixing," *IEEE Signal Process. Mag.*, vol. 19, no. 1, pp. 44–57, Jan. 2002.
[39] H. Kwon and N. M. Nasrabadi, "Kernel matched subspace detectors for hyperspectral target detection," *IEEE Trans. Pattern Anal. Mach. Intell.*, vol. 28, no. 2, pp. 178–194, Feb. 2006.
[40] N. Keshava, "A survey of spectral unmixing algorithms," *Lincoln Lab. J.*, vol. 14, no. 1, pp. 55–78, 2003.
[41] J. M. Bioucas-Dias *et al.*, "Hyperspectral unmixing overview: Geometrical, statistical, and sparse regression-based approaches," *IEEE J. Sel. Topics Appl. Earth Observ. Remote Sens.*, vol. 5, no. 2, pp. 354–379, Apr. 2012.
[42] T. Wang, B. Du, and L. Zhang, "A kernel-based target-constrained interference-minimized filter for hyperspectral sub-pixel target detection," *IEEE J. Sel. Topics Appl. Earth Observ. Remote Sens.*, vol. 6, no. 2, pp. 626–637, Apr. 2013.
[43] S. Kraut, L. L. Scharf, and R. W. Butler, "The adaptive coherence estimator: A uniformly most-powerful-invariant adaptive detection statistic," *IEEE Trans. Signal Process.*, vol. 53, no. 2, pp. 427–438, Feb. 2005.
[44] D. Manolakis, R. Lockwood, T. Cooley, and J. Jacobson, "Is there a best hyperspectral detection algorithm?" *Proc. SPIE*, vol. 7334, pp. 733402-1–733402-3, Apr. 2009. [Online]. Available: http://www.spie.org/app/search/browse?Ntt=Is+there+a+best+hyperspectral+detection+algorithm%3F&Dy=1&Nty=1&Nrpp=20
[45] L. L. Scharf and L. T. McWhorter, "Adaptive matched subspace detectors and adaptive coherence estimators," in *Proc. Conf. Rec. 30th Asilomar Conf. Signals, Syst. Comput.*, vol. 2. 1996, pp. 1114–1117.
[46] Y. Chen, N. M. Nasrabadi, and T. D. Tran, "Hyperspectral image classification via kernel sparse representation," *IEEE Trans. Geosci. Remote Sens.*, vol. 51, no. 1, pp. 217–231, Jan. 2013.
[47] R. Feng, Y. Zhong, and L. Zhang, "Adaptive non-local Euclidean medians sparse unmixing for hyperspectral imagery," *ISPRS J. Photogramm. Remote Sens.*, vol. 97, pp. 9–24, Nov. 2014.
[48] D. Zhang, M. Yang, and X. Feng, "Sparse representation or collaborative representation: Which helps face recognition?" in *Proc. IEEE Int. Conf. Comput. Vis. (ICCV)*, Nov. 2011, pp. 471–478.
[49] T. Zhou, D. Tao, and X. Wu, "Manifold elastic net: A unified framework for sparse dimension reduction," *Data Mining Knowl. Discovery*, vol. 22, no. 3, pp. 340–371, 2011.
[50] L. Zhang, L. Zhang, D. Tao, and X. Huang, "Sparse transfer manifold embedding for hyperspectral target detection," *IEEE Trans. Geosci. Remote Sens.*, vol. 52, no. 2, pp. 1030–1043, Feb. 2014.
[51] B. Du, Y. Zhang, L. Zhang, and D. Tao, "Beyond the sparsity-based target detector: A hybrid sparsity and statistics-based detector for hyperspectral images," *IEEE Trans. Image Process.*, vol. 25, no. 11, pp. 5345–5357, Nov. 2016.
[52] S. S. Chen, D. L. Donoho, and M. A. Saunders, "Atomic decomposition by basis pursuit," *SIAM Rev.*, vol. 43, no. 1, pp. 129–159, 2001.
[53] J. A. Tropp and A. C. Gilbert, "Signal recovery from random measurements via orthogonal matching pursuit," *IEEE Trans. Inf. Theory*, vol. 53, no. 12, pp. 4655–4666, Dec. 2007.
[54] D. L. Donoho, M. Elad, and V. N. Temlyakov, "Stable recovery of sparse overcomplete representations in the presence of noise," *IEEE Trans. Inf. Theory*, vol. 52, no. 1, pp. 6–18, Jan. 2006.
[55] J. A. Tropp, "Greed is good: Algorithmic results for sparse approximation," *IEEE Trans. Inf. Theory*, vol. 50, no. 10, pp. 2231–2242, Oct. 2004.
[56] L. Ma, M. M. Crawford, and J. Tian, "Anomaly detection for hyperspectral images based on robust locally linear embedding," *J. Infr., Millim., Terahertz Waves*, vol. 31, no. 6, pp. 753–762, 2010.

TING WANG received the B.S. degree in photogrammetry and remote sensing from Wuhan University, Wuhan, China, in 2009, and the Ph.D. degree from the State Key Laboratory of Information Engineering in Surveying, Mapping and Remote Sensing, Wuhan University, in 2014. He is currently a Research Associate with the Institute of Space and Earth Information Science, The Chinese University of Hong Kong, Hong Kong. His research interests include hyperspectral image processing, machine learning algorithms, and urban and costal remote sensing applications.

HONGSHENG ZHANG (S'12–M'14) received the B.Eng. degree in computer science and technology and the M.Eng. degree in computer applications technology from South China Normal University, in 2007 and 2010, respectively, and the Ph.D. degree in earth system and geoinformation science from The Chinese University of Hong Kong (CUHK) in 2013.

He is currently a Research Assistant Professor with the Institute of Space and Earth Information Science, CUHK. His research interests are on remote sensing applications in tropical and subtropical areas, with a focus on urban environment and natural disasters monitoring, using multi-source remote sensing data fusion and image pattern recognition techniques.

HUI LIN (M'00–SM'10) received the Diploma degree in aero photogrammetry engineering from the Wuhan Technical University of Surveying and Mapping, Wuhan, China, in 1980, the M.Sc. degree in cartography and remote sensing from the Chinese Academy of Sciences, Beijing, China, in 1983, and the M.A. and Ph.D. degrees in geographic information systems (GIS) from the University at Buffalo, Buffalo, NY, USA, in 1987 and 1992, respectively.

Since 1993, he has been with The Chinese University of Hong Kong (CUHK), Hong Kong, where he is the Chen Shupeng Professor of geoinformation science and the Director of the Institute of Space and Earth Information Science with CUHK. He is also currently the Director of the Hong Kong Base of the National Remote Sensing Center of China. He has authored or co-authored over 200 academic papers, ten books, and one atlas and edited ten conference proceedings. His major research interests are in satellite remote sensing for cloudy and rainy environments, virtual geographic environments, and GIS applications. He is the founding President of the International Association of Chinese Professionals in Geographic Information Science. He has been elected Academician of the International Eurasian Academy of Sciences and the Vice Chairman of the China National Committee of International Society of Digital Earth. He is the Chief Editor of the international journal *Annals of GIS*.

XIUPING JIA (M'93–SM'03) received the B.Eng. degree from the Beijing University of Posts and Telecommunications, Beijing, China, in 1982, and the Ph.D. degree in electrical engineering from the University of New South Wales, Sydney, NSW, Australia, in 1996.

Since 1988, she has been with the School of Engineering and Information Technology, University College, Australian Defense Force Academy, University of New South Wales, Canberra, BC, Australia, where she is currently a Senior Lecturer. She is also a Guest Professor with Harbin Engineering University, China, and an Adjunct Researcher with the China National Engineer Research Center for Information Technology in Agriculture. She is the co-author of the remote sensing textbook titled *Remote Sensing Digital Image Analysis* [Springer-Verlag, 3rd (1999) and 4th eds. (2006)]. Her research interests include remote sensing, imaging spectrometry, and spatial data analysis.

Dr. Jia is an Editor of the *Annals of GIS* and an Associate Editor of the IEEE TRANSACTIONS ON GEOSCIENCE AND REMOTE ENSING.